UCLA
UCLA Previously Published Works

Title
Microchannel cooling device with perforated side walls: Design and modeling

Permalink
https://escholarship.org/uc/item/6qt5051j

Authors
Warrier, Gopinath R
Kim, Chang-Jin
Ju, Y Sungtaek

Publication Date
2014

DOI
10.1016/j.ijheatmasstransfer.2013.09.022

Peer reviewed

eScholarship.org Powered by the California Digital Library
University of California

International Journal of Heat and Mass Transfer 68 (2014) 174–183

Contents lists available at ScienceDirect

International Journal of Heat and Mass Transfer

journal homepage: www.elsevier.com/locate/ijhmt

Microchannel cooling device with perforated side walls: Design and modeling

Gopinath R. Warrier *, Chang-Jin Kim, Y. Sungtaek Ju

Mechanical and Aerospace Engineering Department, University of California, Los Angeles, CA 90095, USA

ARTICLE INFO

Article history:
Received 23 April 2013
Received in revised form 11 September 2013
Accepted 12 September 2013

Keywords:
Electronics cooling
Microchannel
High heat flux

ABSTRACT

We propose and analyze a novel two-phase microchannel cooling device that incorporates perforated side walls for potential use as an embedded thermal management solution for high heat flux semiconductor devices. A dense array of perforated side walls separate alternating liquid and vapor microchannels, allowing the vapor generated through evaporation of liquid supplied through micro-perforations to flow only in the dedicated vapor channels. By separating the liquid and vapor flows, these "perspiring" side walls enable us to circumvent flow instabilities and other challenges associated with conventional two-phase microchannel cooling while at the same time effectively take advantage of the large extended surface areas available in high-aspect-ratio microchannels. One implementation of our design is parametrically analyzed using finite element modeling, demonstrating the potential of our proposed device for handling high heat flux electronic and optoelectronic semiconductor devices.

© 2013 Elsevier Ltd. All rights reserved.

1. Introduction

Continued miniaturization and increasing power ratings of electronic and optoelectronic devices have resulted in the need for active embedded cooling techniques with high heat flux removal capability. Flow boiling in microchannels has received a lot of attention for its promise in handling ultra-high heat fluxes [1–12]. Practical applications of flow boiling in microchannels for semiconductor device cooling, however, remain challenging due to issues related to flow instabilities, complexity of two-phase flow regimes, and excessive pressure drops associated with inlet constrictions. Ability to initiate and localize bubble nucleation in a controlled manner may help partially mitigate some of these challenges but such ability remains elusive for most dielectric fluids with very high wettability.

An alternative approach involves separating the liquid and vapor phases as an intrinsic part of the device design to help alleviate some of the difficulties. An early attempt by David et al. [13] placed a hydrophobic "breather" membrane on conventional microchannels to partially separate water vapor from liquid water and thereby mitigate flow instabilities. In this study, flow boiling in microchannels with a 65 µm thick porous PTFE membrane (with 220 nm pores) separating the liquid channels from the vapor channels was investigated. The device had 19 channels machined out of copper with each channel being 19 mm long. The liquid microchannels were 130 µm wide and 134 µm deep, while the mating vapor channel were 125 µm wide and 132 µm deep. Experiments were performed with water as the test fluid. A thermofluid model for the device (vented and non-vented) was also developed to predict the performance. The experiments showed that with vapor venting, the quality of the two-phase flow in the microchannels was lower. Experimental results showed that compared to a non-venting device, the venting device had ~60% reduction in the pressure drop. Model predictions matched well with the experimental results, except at higher mass flow rates (>600 kg/m^2 s) where the model overpredicts the pressure drop. This was attributed to the formation of churn-annular flow pattern observed at high mass fluxes. Additionally, no two-phase flow instabilities were observed in these experiments.

In these experiments, heat fluxes up to 70 W/cm^2 were used. For low mass flux, the heat transfer coefficients measured for the vented device was lower than that for the non-vented device. On the other hand at higher mass fluxes, the heat transfer coefficients for the vented device were approximately the same or slightly higher than those measured for the non-vented device. Though the vapor quality in the microchannels were lower in the case of the vented device, the reduction in the fluid saturation temperature (due to reduction in the pressure drop, up to 4.4 °C) and changes in the flow regime resulted in the heat transfer rates being similar to that obtained for the non-vented device. Due to lower vapor quality, stratified flow was typically obtained which generally has lower heat transfer rates compared to annular or churn-annular flows. The model predictions matched the experimental results quite well, except at the lowest mass flux where they were overpredicted. Though the experimental results obtained using the

* Corresponding author. Tel.: +1 310 825 9617.
E-mail address: gwarrier@ucla.edu (G.R. Warrier).

0017-9310/$ - see front matter © 2013 Elsevier Ltd. All rights reserved.
http://dx.doi.org/10.1016/j.ijheatmasstransfer.2013.09.022

vented-device did not show much improvement in the heat transfer rates compared to the non-vented device, the results did show a clear reduction in the pressure drop characteristics. The authors hypothesized that the much higher heat transfer rates could be realized with small liquid channel and very large vapor channels separated by a porous membrane. Since evaporation does not take place within (or on the surface of) the membrane, this approach relies on passive transport of vapor across the channels and then across the membrane, which can be inefficient and incomplete. The lack of comparable "hydrophobic" membranes, furthermore, makes this approach difficult to apply for well wetting dielectric fluids.

In another recent study, Narayanan et al. [14] proposed using a "nano-porous patch", where a thin porous membrane is used to separate the vapor from a thin evaporating liquid layer of a controlled thickness. A gas jet was used to assist the removal of the vapor generated. Both modeling and experiments were conducted. Modeling results showed that the heat transfer rates increase with decrease in liquid film thickness and/or membrane thickness. Increase in the air flow rate also increases the heat transfer rate. With liquid and membrane thicknesses of 1 μm, heat fluxes of ~700 W/cm^2 were possible with FC-72 as the test liquid. Results for water were consistently lower by factors of 2.2–3.

To validate the model results, experiments were conducted with water as the test fluid. In these experiments, liquid film thicknesses of 200 and 400 μm were tested with a 60 μm thick membrane with 20 nm pores (porosity = 50%). Since the location of the liquid–vapor interface is a key input parameter in the model, and because it could not be measured in the experiments, two extreme cases were considered – one where the liquid completely fills the membrane (i.e., evaporation occurs at the membrane outlet) and the other where the membrane is completely filled with vapor (i.e., evaporation occurs at the membrane inlet). Experiments show that compared to single-phase air jet cooling, evaporative cooling enhance heat transfer by a factor of 2. For surface temperature above 70 °C, the experimental results were in agreement with model predictions. At lower wall temperature, the models underpredict the experimental results. This discrepancy was attributed to leakage through the membrane.

The results from [14] show that as high heat flux removal can be achieved with evaporative cooling. Moreover, with the porous membrane completely filled with liquid, the resistance to mass transfer is minimized resulting in the highest heat transfer rates. The "horizontal" porous patch cooling device implemented in [14], however, suffered from important limitations. The liquid layer defined by the porous membrane has to be kept very thin (~1 μm) because the thermal energy needs to be first conducted across this liquid layer. Such a thin liquid layer, however, presents significant hydraulic resistance to the flow parallel to the membrane, leading to an excessive pressure drop. The horizontal configuration of the cooling device also limits the heat transfer surface area to only that of the exposed heat source.

In this article, we propose a novel two-phase microchannel cooling device with perforated side walls. This device helps circumvent the limitations of the previous cooling device by decoupling the main heat conduction paths (along the microchannel walls) from the liquid supply paths (along dedicated "wide" liquid channels) and by taking advantage of large extended surfaces available in high-aspect-ratio microchannel walls for evaporation heat transfer. We provide details of one practical implementation of the device concept and thermofluid modeling results.

The cooling device proposed in this study involves a situation very similar to that studied in [14], where the porous side wall is completely filled with liquid and evaporation occurring at the vapor channel. Subsequently, mass transfer resistance is expected to be negligible. The results from [13,14] show that the inclusion of a porous membrane to separate the liquid and vapor flow paths improves the heat transfer and pressure drop characteristics of cooling devices that involve boiling or evaporation. An additional benefit of separating the two phases is the mitigation of instabilities related to the pressure drop. Due to the differences in the geometry and the operating conditions, it is not possible to compare the data obtained from these studies to the numerical simulation results obtained in this study. However, the modeling methodology adopted and the performance of the devices in the two studies discussed above shows that the concept of our high heat flux cooling device and the thermofluid modeling approach used are appropriate.

2. Cooling device concept

We propose a novel embedded evaporative cooling device based on phase-separated microchannels with perforated ("*perspiring*") side walls for the thermal management of ultra-high heat flux devices. A schematic of this device is shown in Fig. 1. In this cooling device, each liquid channel is separated from the two adjacent vapor channels by side walls that contain arrays of micro perforations. Liquid flowing in the liquid channels is transported through the perforations by capillary action and evaporate into the vapor channels to efficiently remove heat. Conceptually, our approach may loosely be viewed as a geometric adaptation of transpiration cooling systems investigated to tackle demanding thermal management challenges of hypersonic vehicles. Our unique perforated channel walls of high aspect ratio offer dual benefits by serving both as extended heat transfer surfaces (fins) and as micro-porous membranes for phase separation.

We select silicon as our channel wall material in part to take advantage of its unique micromachinability, such as photo-electrochemical (PEC) etching and deep reactive ion etching (DRIE). This also helps ensure that our "embedded" cooling solution is compatible with recent trends towards heterogeneous integration of high-power-density circuits built on SiC or diamond substrates with silicon-based CMOS circuits. Examples of the former may include GaN-based microwave or RF power amplifiers and other power switching/control devices, and high-performance microprocessors. Major R&D efforts are currently under way to prepare GaN [15] devices on diamond substrates. The relatively small mismatch in CTEs between Si and SiC and between Si and diamond helps reduce thermal stress on the microchannels during thermal cycling.

The microfabrication processes considered for our cooling device can be scaled up to create multiple microchannel groups on a single substrate to cover large areas. Alternatively, multiple cooling devices may be placed side to side to handle an array of chips over a large area.

3. Coolant selection and its thermophysical properties

The peak junction temperature specified for wide-bandgap GaN devices is typically over 200 °C. Previous modeling and depth-resolved Raman measurements showed, however, that a large portion of the temperature drop occurs across the device buffer layers and interfaces rather than the substrate [16]. With a target top "substrate" temperature of 90 °C, we choose as our working fluid Fluorinert™ FC-72 with a boiling point of 56 °C (at 1 atm) and with material compatibility superior to hydrofluoroethers (HFEs). Different Fluorinert fluids with higher boiling points (e.g., FC-77 at 97 °C) may be used instead if higher condenser temperatures are desired.

Heterogeneous bubble nucleation generally occurs at microscopic cavities that entrap gas [17] and the wall superheat required

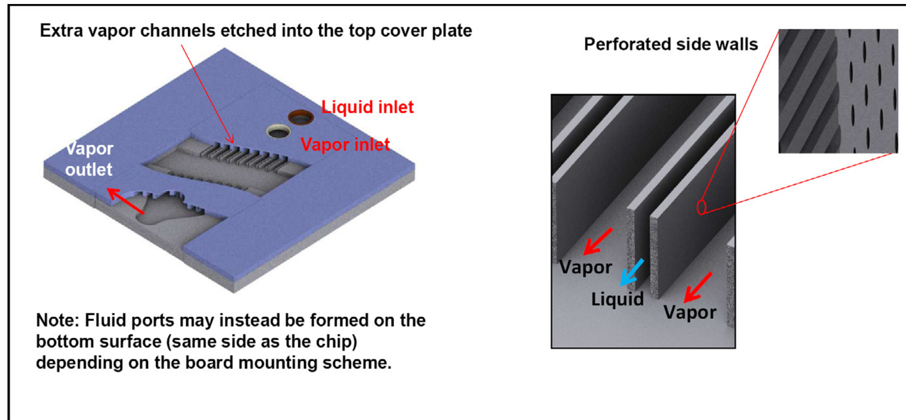

Fig. 1. A schematic of the proposed embedded evaporative cooling device featuring phase-separated microchannels with perforated side walls. (Features not to scale).

for bubble nucleation has been modeled in various studies [18,19]. In the prevailing model, the wall superheat required for Onset of Nucleate Boiling (ONB) can be predicted as,

$$T_{w,\mathrm{ONB}} - T_{sat} = \frac{4\sigma T_{sat}}{D_c \rho_v h_{fg}} \tag{1}$$

where σ is the surface tension, D_c is the cavity mouth diameter (modified to account for contact angle) [19], and ρ_v and h_{fg} are the vapor density and latent heat of evaporation of the fluid, respectively. Fluids with low surface tension (well wetting fluids like FC-72 used in the present work) make it harder for cavities to trap gas. Additionally, smaller cavities require larger wall superheats to nucleate. Furthermore, even if bubbles do nucleate and grow, the vapor would be vented out to the vapor channel through the pores rather than growing in the liquid channel against the pressure. In the present study, for FC-72 at atmospheric pressure and a contact angle of 10°, the predicted wall superheat required for nucleation is about 62 °C (wall temperature $\simeq$ 120 °C). For the wall temperatures expected in this study, nucleation is not expected to occur [20-21].

High-aspect-ratio microchannel geometry will allow us to achieve significant enhancement in the effective heat transfer coefficient (per fin base area) over that of micro-gap flows between *non-finned* non-porous flat surfaces [21]. The thermal energy is conducted along the perforated solid walls and then transferred to the evaporating liquids in the micro-pores in our microchannel device, which helps minimize the negative impact of the low thermal conductivity of a dielectric fluid.

For realistic thermofluid modeling of the chip/cooling device, accurate thermodynamic and transport properties of FC-72 are necessary. The properties of liquid FC-72, such as density (ρ), thermal conductivity (k), specific heat capacity at constant pressure (C_p), viscosity (μ), and surface tension (σ) are readily available [22]. However, many thermophysical properties of the vapor of FC-72 are not available in the literature.

We develop models to predict some of the missing vapor properties required for the thermofluid modeling, focusing on near atmospheric pressures. A four-parameter equation of state (EOS) [23,24] is used to predict ρ and c_p of saturated and superheated FC-72 vapor. This EOS evaluates the pure component parameters using the critical temperature (T_c), critical pressure (P_c) and the accentric factor (ω). The EOS is given as,

$$P = \frac{RT}{(V-b_1)} - \frac{a(T)}{(V-b_2)(V+b_3)} \tag{2}$$

where

$$\begin{aligned}
B_1 &= 0.08974 - 0.03452\omega + 0.00330\omega^2 \\
B_2 &= 0.03686 + 0.00405\omega - 0.01073\omega^2 + 0.00157\omega^3 \\
B_3 &= 0.15400 + 0.14122\omega - 0.00272\omega^2 - 0.00484\omega^3 \\
A &= 0.44869 + 0.04024\omega + 0.01111\omega^2 - 0.00576\omega^3 \\
\alpha &= 0.1070 + 1.3787\omega - 0.2933\omega^2 \\
s &= \tfrac{AR^2T_c^2}{P_c} \\
b_i &= \tfrac{B_iRT_c}{P_c}, \quad i = 1,2,3 \\
a(T) &= s\left[1 + \alpha(1 - \sqrt{T_r})\right]^2
\end{aligned} \tag{3}$$

Here, P is the pressure (Pa), V is the specific volume (m^3/mol), T is the temperature (K) and R is the universal gas constant. We use molecular weight (M) = 338 g/mol, ω = 0.5034, P_c = 18.68 bar, T_c = 449 K, and critical density (ρ_c) = 557.7 kg/m^3 (for Perfluoro-n-Hexane [25], which is the pure form of FC-72). For a given T and P, an iterative process is used to solve for the roots of EOS given in Eq. (2); this process is used to determine both the saturated and superheated vapor specific volume. In addition, the vapor specific heat capacity is evaluated using Eq. (3) and the specific enthalpy departure function $(H - H^0)_T$ reported in [23]:

$$\frac{(H-H^0)_T}{RT_c} = \frac{Z}{T_r} - T_r + \frac{1}{(B_2+B_3)}\left[a(T_r) - T_r\frac{da(T_r)}{dT_r}\right]\ln\left[\frac{Z-B_2P_r/T_r}{Z+B_3P_r/T_r}\right] \tag{4}$$

where the compressibility (Z) is given as,

$$Z = \frac{PV}{RT} \tag{5}$$

The C_p of vapor is then calculated as,

$$C_p = C_p^0 + \left.\frac{\partial(H-H^0)_T}{\partial T}\right|_P \tag{6}$$

where C_p^0 is the ideal gas specific heat at constant pressure.

The transport properties of the vapor (μ and k) are predicted using the models described in [26–28]. The vapor viscosity is given by the following relations:

Viscosity of low-pressure gas [26]:

$$\begin{aligned}
\mu^0\xi &= 4.610T_r^{0.618)} - 2.04\exp(-0.449T_r) + 1.94\exp(-4.058T_r) + 0.1\xi \\
&= 0.217T_c^{1/6}M^{-1/2}P_c^{-2/3}
\end{aligned} \tag{7}$$

where P_c is the critical pressure in MPa and μ^0 is the viscosity in micropoise.

Table 1
Comparison of the measured and predicted densities of saturated FC-72 liquid.

p (bar)	ρ [19] (kg/m^3)	p (Predicted) (kg/m^3)
0.8	1607.8	1644.6
1.0	1590.5	1616.1
1.2	1579.8	1585.6

Table 2
Predicted properties of FC-72 vapor at the atmospheric pressure.

$T - T_{sat}$ (K)	ρ (kg/m^3)	k ($\times 10^3$) (W/m K)	C_p (J/kg K)	μ ($\times 10^6$) (Pa s)
0	13.2	23.2	895.2	12.40
5	13.0	23.7	907.9	12.56
10	12.8	24.2	920.6	12.73
20	12.4	25.0	946.0	13.08
30	11.9	26.4	971.4	13.44
40	11.6	27.6	996.8	13.79

Viscosity of dense-gas [27]:

$$\left[(\mu - \mu^0)\xi + 1\right]^{1/4} = 1.0230 + 0.23364\rho_r + 0.58533\rho_r^2 - 0.40758\rho_r^3 + 0.093324\rho_r^4 \quad (8)$$

Thermal conductivity of low-density gas [23]:

$$k^0 = \frac{(C_v^0 + 4.47)\mu^0}{M} \quad (9)$$

where C_v^0 is the specific heat at constant volume for an ideal gas.

Thermal conductivity of dense-gas [28]:

$$\begin{aligned}(k - k^0)\xi Z_c^5 &= 14.0x10^{-8}[\exp(0.535\rho_r) - 1] \quad for\, \rho_r < 0.5\\ (k - k^0)\xi Z_c^5 &= 13.1x10^{-8}[\exp(0.67\rho_r) - 1.069] \quad for\, 0.5 < \rho_r < 2.0\\ (k - k^0)\xi Z_c^5 &= 2.976x10^{-8}[\exp(1.155\rho_r) + 2.016] \quad for\, 2.0 < \rho_r < 2.8\end{aligned} \quad (10)$$

In the above equations, T_r, P_r and ρ_r are the reduced temperature (=T/T_c), pressure (=P/P_c) and density (=ρ/ρ_c), respectively.

A computer code written in MATLAB is used to perform all the calculations. To validate the models developed, we compare the predicted saturated liquid density with those obtained using correlations [22]. Good agreement is obtained as shown in Table 1, for pressures varying from 0.8 to 1.2 bar. Table 2 lists the predicted saturated and superheated vapor properties for atmospheric pressure (P = 1.01325 bar). The superheats ($T - T_{sat}$) vary from 0 to 40 K; these cover the range of superheats that are expected in the thermofluid model.

4. Micro–macro thermofluid modeling

To help illustrate the performance of our cooling device concept, we consider one specific implementation and model its performance using full 3D finite element simulations. Key channel dimensions (and their potential ranges) are chosen based on the known and expected capabilities of DRIE (deep reactive ion etching) and PEC (photoelectrochemical etching) on silicon wafers. A possible microfabrication approach of the microchannels with perforated side walls is discussed in Section 6. The two design parameters that we vary parametrically in this design are the liquid and vapor channel widths. The design parameters of the cooling device we modeled are as follows:

- Channel wall height: 350 μm (fixed)
- Main channel length: 2.5 mm (fixed)
- Vapor channel width: varied from 60 to 120 μm
- Liquid channel width: varied from 20 to 60 μm
- Channel side wall thickness: 30 μm (fixed)
- Channel side wall porosity: 20% (fixed)
- Channel side wall pore diameter: 1.5 μm (fixed)

A side wall porosity of 10–20% is chosen as a compromise between the thermal conductivity and mechanical strength of the side walls. A potential range of the sidewall porosity, which may be viewed as the ratio of the total exposed area of the micro-perforations to the total area of the sidewall, was specified primarily from our expected limitation on microfabrication. Much higher porosity values would also be undesirable as they lead to severe degradation in the side wall thermal conductivity and mechanical strength. The thermal conductivity of perforated silicon plates at a porosity of 20% is estimated to be approximately 70 W/m K at 70 °C based on the previous measurement data on thin membranes [29,30] after the size effect on phonon transport is accounted for. For a wall thickness of 30 μm and a local heat transfer coefficient of 10^4 W/m^2 K (based on micro-pore modeling), the corresponding fin thermal decay length $(kA/hP)^{1/2}$ is approximately 450 μm.

It is important to not the fact that our device is designed specifically to address the issue of high heat flux removal in high-performance electronic devices, including power amplifiers. We note that the modeling was only done for a unit cell (one vapor and one liquid channel pair). Power dissipated will be proportionately higher for actual devices that contain a large number of parallel channels.

4.1. Overall modeling approach

A semi-coupled micro–macro thermofluid modeling study is used to predict both the heat transfer performance and pressure drop characteristics of the cooling device. As the first step, we developed a model to predict the evaporative heat and mass flux in a single micro-perforation under a prescribed wall superheat. The predicted evaporation heat transfer coefficient (after being corrected to account for the finite porosity of the side walls) was then input into a 3D FEM model of one period of the phase-separated channel assembly to predict the electronic device temperature and related pressure drops. The relevant conservation equations are solved for both the liquid and vapor channels, with the evaporative mass flux (calculated from the evaporative heat transfer coefficient obtained from the micro-pore model) used as a source/sink term to couple the flows on the two sides of the perforated side wall. Note that this is a conjugate heat transfer problem as heat conduction through all walls is explicitly accounted for in this model.

4.2. Micro-pore model

We solved the mass, momentum, and energy equations in 2D axisymmetric coordinates for a single micro-pore to determine the evaporation heat and mass flux under a prescribed wall superheat. The liquid–vapor interface was captured using the Level-Set (LS) method. Details of the numerical simulation scheme can be found elsewhere [31,32] and will not be discussed in detail. Briefly, Fig. 2 shows the computational domain used for the simulations. The walls of the perforation are held at a constant temperature (T_w) and the liquid entering the perforation (at the bottom) is assumed to be at its saturation state. All velocity gradients at the bottom (inlet) are set equal to zero. The liquid–vapor interface is assumed to be at the saturation temperature (T_{sat}). At the start of each simulation, the liquid–vapor interface was positioned in the middle of the micro-perforation. The location of the interface does not influence the results obtained. Once simulations begin (i.e., heating begins), the shape and location of the interface adjust themselves in response to evaporation at the interface. In these simulations, the contact angle is prescribed. Contact angle

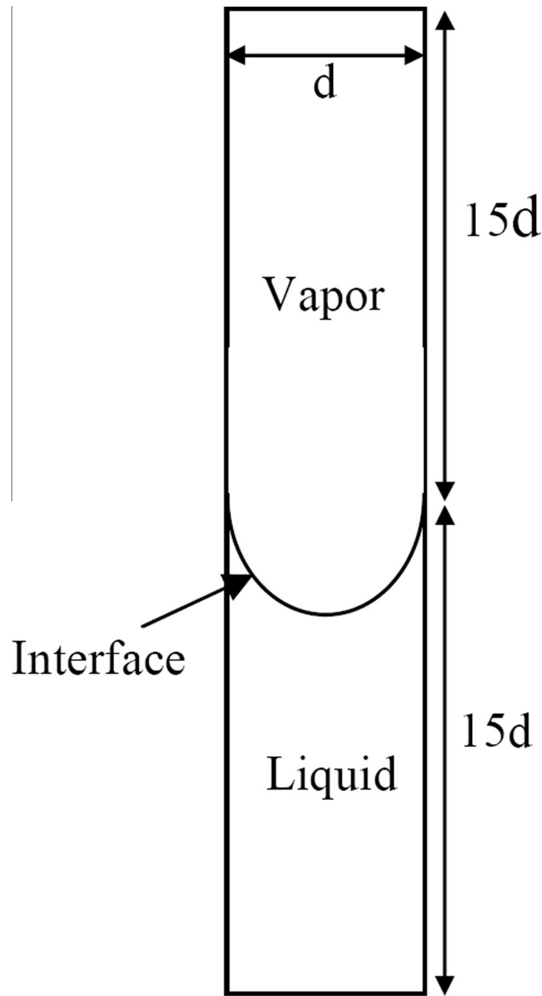

Fig. 2. Computational domain for micro-pore simulations.

hysteresis is not accounted in the simulations. As the interface movement is by evaporation and condensation rather than a physical force, making contact angle hysteresis not important. The magnitude of the hysteresis is also expected to be small for well-wetting liquids. Additionally, the contact angle hysteresis was not accounted for because we were primarily interested in the steady (static) performance of the device in the present study. We instead varied the contact angle for a parameter study. Future studies will investigate dynamic responses (start up and varying heat dissipation) where contact angle hysteresis may play a role. The simulations were then continued until a steady-state was achieved. The effective evaporation heat transfer coefficient, h_{evap}, is calculated as,

$$h_{evap} = \frac{\int q_{evap} dA_{\text{int}}}{(T_w - T_{sat}) A_{pore}} \tag{11}$$

where q_{evap} is the local interfacial heat flux over the interfacial area dA_{int} and A_{pore} is the cross-sectional area of the micro-perforation (=$\pi d^2/4$).

4.3. Microchannel model

Heat transfer and fluid flows in the phase separated microchannel array were modeled using the finite element method. Due to significant computational requirements involved in solving 3D flow and conjugate heat transfer problems, we only modeled a single period of the channels (one liquid channel and the two halves of the adjacent vapor channels). The computational domain (cross-sectional and top views) for the simulations is shown in Fig. 3. We note that, by not allowing heat spreading in the transverse direction, this unit-cell model may significantly underpredict the real-world performance for cooling semiconductor chips of finite widths.

The micro-perforations were not directly modeled in the microchannel model. The evaporation of the liquid in the perforations is accounted for using an effective evaporation heat transfer coefficient. Corresponding mass sink/source terms were included at the respective channel wall surfaces to represent mass loss/gain due to evaporation.

The SiC chip (semiconductor device) is mounted on top of the cooling device. The chip is 0.5 mm in length and is located 0.5 mm from the edge of the channels in the simulation domain. An infinitely wide (in the transverse direction) heat source of length 100 μm (in the streamwise direction) is applied on the chip surface at a constant heat flux of 1000 W/cm^2.

As mentioned earlier, all channel dimensions are fixed except the widths of the liquid and vapor channels, denoted by W_l and W_v, which were varied parametrically. Most simulations were performed for two different values of h_{evap} (=10 kW/m^2 K and 20 kW/m^2 K). In a few select cases h_{evap} was varied in the range 5–30 kW/m^2 K to examine its impact. The values obtained from the numerical simulation of the micro-perforations is corrected to account for both the accommodation coefficient and the sidewall porosity. Note that for vaporization from a liquid–vapor interface, we use the accommodation coefficient as the ratio of the net mass flux at the interface to the mass flux at an interface with no recondensation. It is always less than unity. The resultant overall effective heat transfer coefficient is then used in the thermofluid model. This provides a lower bound for the effective heat transfer coefficient. The change in the saturation temperature due to the pressure drop along the microchannels is negligible and was hence not accounted for.

No slip conditions were applied at all walls. Zero temperature gradients (negligible conductive heat flux) were specified at the inlets and outlets of the channels. All the other surfaces were assumed to be thermally insulated. A uniform pressure boundary condition was specified at the liquid inlet and the vapor outlet.

5. Results and discussion

5.1. Micro-perforations

We considered two different micro-pore diameters (1 and 2 μm) and two different contact angles (5° and 10°). For a fixed wall superheat of 7 K, the predicted effective heat transfer coefficients for the two different pore diameters and the two different contact angles are listed below in Table 3. Fig. 4 shows the predicted dimensionless temperature profile (=$(T - T_{sat})/(T_w - T_{sat})$) in the liquid and the predicted flow field during evaporation from a 1 μm diameter pore with a contact angle of 5°. Note that the majority of evaporation occurs in a relatively small area (thin film

Table 3
Predicted evaporative heat transfer coefficients of a micro-perforation and its array.

Pore diameter (μm)	Contact angle (deg.)	Pore-level evaporative heat transfer coefficient (kW/m^2 K)	Heat transfer coefficient of the wall after porosity correction (kW/m^2 K)
1	5	170	34
	10	160	32
2	5	80	16
	10	70	14

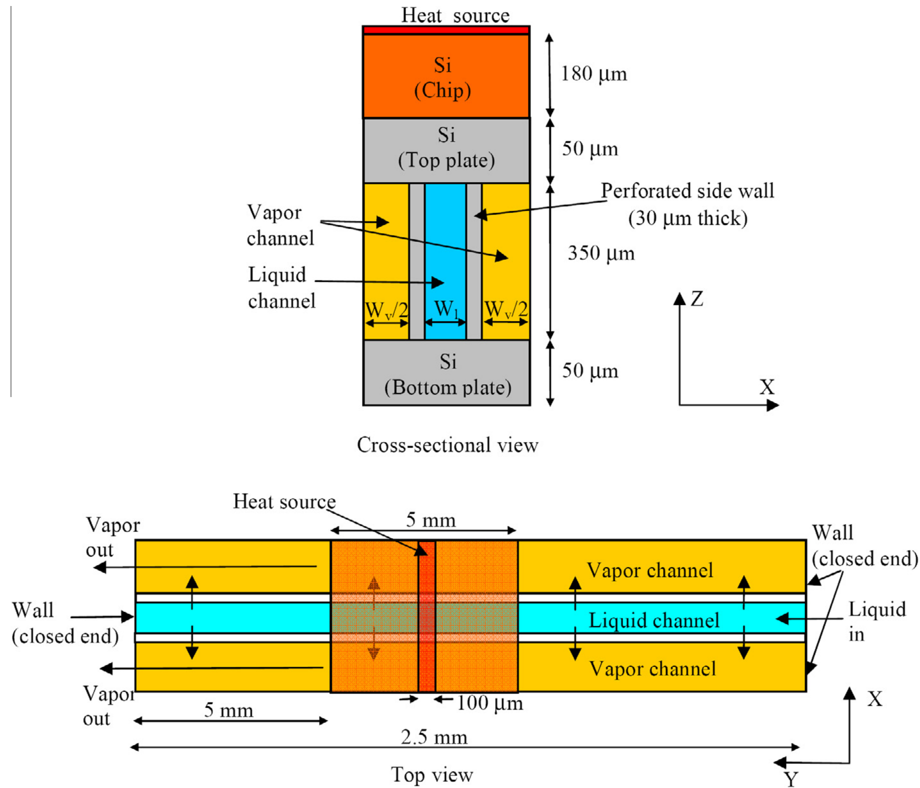

Fig. 3. Computational domain used in our microchannel modeling.

region) close to the solid–liquid–vapor triple-point. For a given pore diameter, increasing the contact angle results in decrease in the effective evaporation heat transfer coefficient. This is due to the fact that lower contact angles lead to thinner films close to the triple-point, which in turn increases the evaporation rate. Additionally, for a given contact angle, increasing the pore-diameter results in a decrease in the evaporation heat transfer coefficient due to the increase in the area of the interface where the local heat transfer rates are relatively low. The effective heat transfer coefficients of the side walls are reduced by finite porosity (factor of 0.2 in our initial design) under the assumption that all pores function independently. The accommodation coefficient is assumed to be 0.05 as a conservative estimate. A preliminary analysis of the evaporation heat transfer performance of Novec fluids on Cu micro-posts [33] suggested higher values for the accommodation coefficient of a dielectric fluid.

5.2. Microchannels

5.2.1. Peak temperature rise

Fig. 5 shows the peak temperature rise in the semiconductor chip ($\Delta T_{peak} = T_{peak} - T_{sat}$) as a function of W_l and W_v. Fig. 5a shows ΔT_{peak} as a function of W_v for a fixed value of W_l (=40 μm). The results are shown for both h_{evap} = 10 and 20 kW/m^2 K. Irrespective of the value of h_{evap}, ΔT_{peak} increases linearly with increase in W_v. This is because the total power supplied increases linearly with increasing W_v. Recall that the heat flux was held constant (1000 W/cm^2). As expected, the peak temperature rise ΔT_{peak} decreases with increasing h_{evap}. A similar trend is observed in Fig. 5b where ΔT_{peak} is shown as a function of W_l for a fixed value of W_v (=60 μm).

For fixed vapor and liquid channel widths, the dependence of ΔT_{peak} on h_{evap} is shown in Fig. 6, for the range 5–30 kW/m^2 K. The peak temperature rise ΔT_{peak} decreases monotonically with increasing h_{evap}. As is well known for heat transfer in extended surfaces, there is competition between heat conduction along the channel side walls, which increases effective convective heat transfer surface areas, and heat loss by evaporation. The peak temperature rise does not decrease significantly once h_{evap} exceeds approximately 20 kW/m^2 K.

As a comparison, the peak temperature rise predicted for single-phase microchannel flows (W_l = 40 μm, W_v = 60 μm) is 28 K, almost twice that for the proposed cooling device, even for a pressure drop as high as 1000 Pa.

5.2.2. Pressure drop

The predicted pressure drop along the liquid microchannel (ΔP_l) is plotted in Fig. 7. Referring to Fig. 7a, it can be seen that ΔP_l increases linearly with W_v. This is once again because the total applied heating power and hence the evaporation rate increases with increase in W_v. The increased liquid mass flow rate (required to compensate for the increased evaporation rate) in turn leads to increase in ΔP_l. Recall that, for laminar flows, $\Delta P \propto v/(D_h)^2$, where v = mean velocity and D_h = hydraulic diameter of the microchannel. Also, for given W_l and W_v, increasing h_{evap} leads to increase in the evaporation rate and hence ΔP_l.

When, instead, W_v is fixed and W_l is varied (Fig. 7b), the pressure drop along the liquid channel ΔP_l decreases with increasing W_l. Since the channel height is much larger than the channel widths considered, the hydraulic diameter scales approximately as $D_h \sim W_l$. One might therefore expect ΔP_l to decrease as $1/W_l^2$. The actual dependence is closer to $\Delta P_l \sim 1/W_l$ because the total power and hence the required mass flow rate increases with W_l. For a given channel geometry, increasing h_{evap} leads to increase in the mass flux and hence ΔP_l.

The pressure drop along the vapor microchannels (ΔP_v) is shown in Fig. 8. Referring to Fig. 8a and b, it is clear that the trends observed are similar to that seen in Fig. 7. Irrespective of the value of h_{evap}, ΔP_v increases linearly with W_l due to corresponding

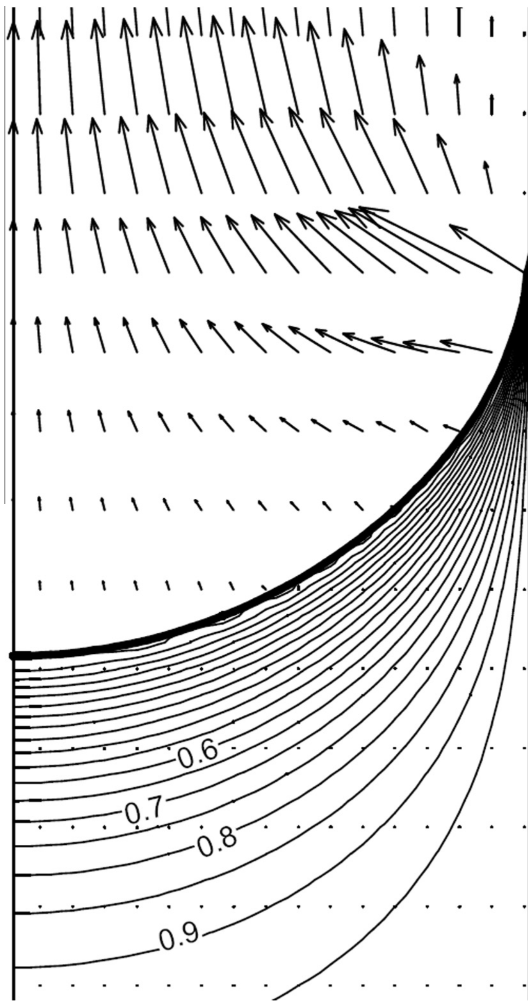

Fig. 4. Predicted flow field and dimensionless temperature contours for a single micro-pore.

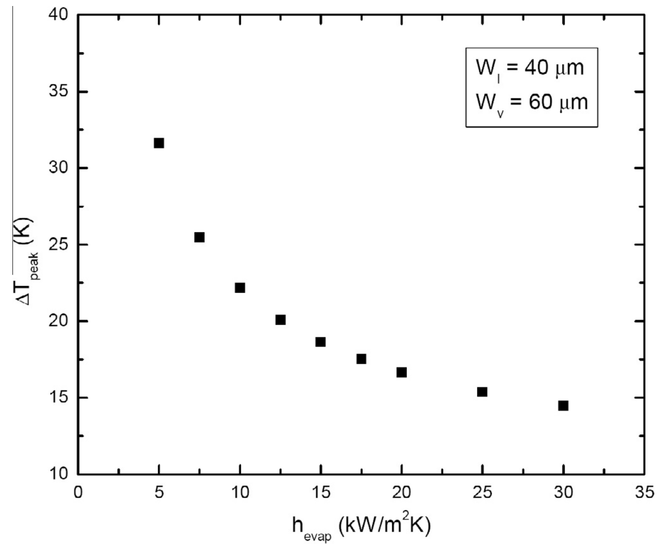

Fig. 6. Variation of ΔT_{peak} with h_{evap}, for fixed W_l and W_v.

increase in the total applied heating power. ΔP_v decreases with increasing W_v and hence the hydraulic diameter but, once again, not as fast as $1/W_v^2$.

The pressure drops in the liquid and vapor microchannels as a function of h_{evap} are plotted in Fig. 9, for W_l = 40 μm and W_v = 60 μm. For the given channel dimensions, increase in h_{evap} results in the increase in both ΔP_l and ΔP_v. Increase in h_{evap} results in increase in the evaporation rate, which in turn raises the liquid and vapor mass flow rates. Consequently, both ΔP_l and ΔP_v increase with increasing h_{evap}.

The calculated pressure profiles for both the liquid and vapor flows are shown in Fig. 10 for $W_l = W_v$ = 60 μm. In the liquid microchannel, the liquid pressure drops approximately linearly just downstream of the inlet; this is consistent with predictions obtained for single-phase laminar microchannel flows. Further down-

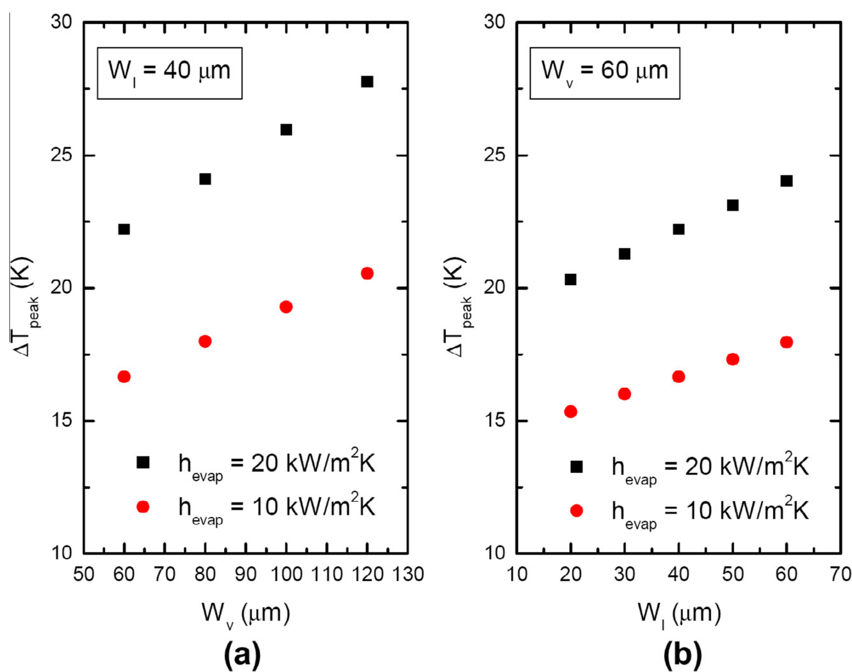

Fig. 5. Variation of ΔT_{peak} as a function of (a) W_v and (b) W_l.

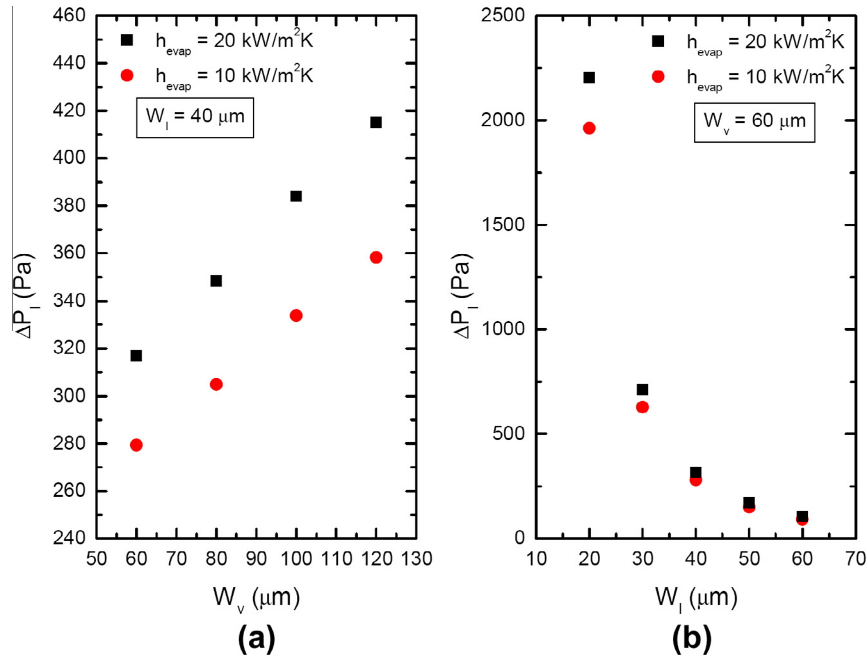

Fig. 7. Predicted ΔP_l as a function of (a) W_v and (b) W_l for two different values of the evaporation heat transfer coefficient.

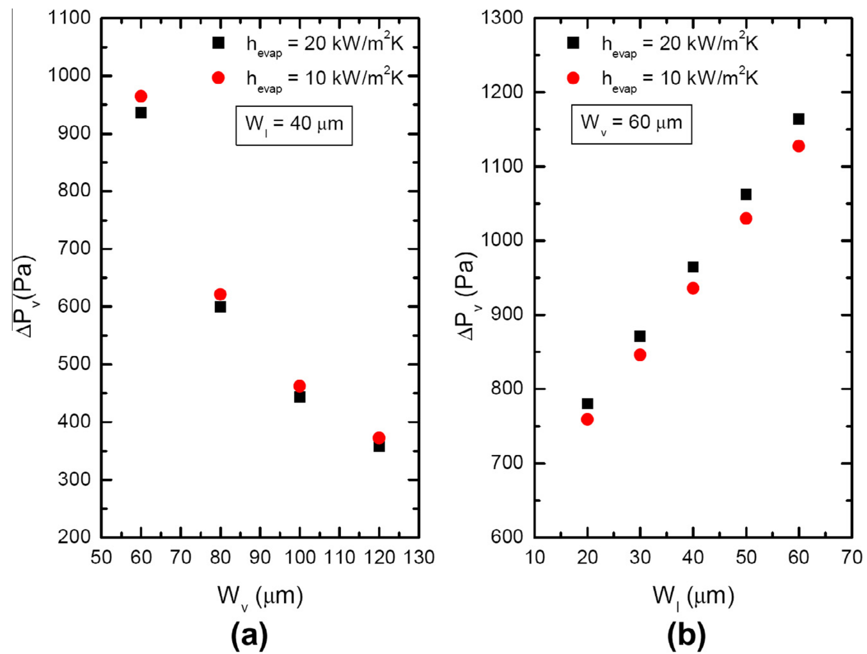

Fig. 8. Predicted ΔP_v as a function of (a) W_v and (b) W_l for two different values of the evaporation heat transfer coefficient.

stream, the pressure decreases more and more gradually because the liquid mass flow rate decreases due to evaporation. In contrast, for the vapor microchannel, the vapor pressure stays approximately constant until the channel wall temperature becomes high enough near the heat source to generate significant vapor.

As mentioned earlier, the pressure drop in the micro-perforations is not included in the thermofluid modeling. The pressure drop was only calculated for a single micro-perforation as part of the numerical simulations performed to determine the evaporative heat flux. As a result, the total pressure drops obtained in this study is lower than could be expected in the actual cooling device. Liquid flows along the perforations are driven primarily by capillary pressure, which is larger than the viscous pressure drop even at the maximum heat flux, rather than the external pressure gradients imposed along or across the micro-channels. Please note again the 'perspiring' side wall was modeled using the effective heat and mass sink terms in our simulations with no pressure drop along the perforations explicitly coming into play.

5.2.3. Dry out

To prevent dry out, the capillary driving force must be sufficient to overcome frictional pressure loss along the perforations. For pore diameters ranging from 1 to 2 μm, our modeling results show that the capillary pressure ranges from 39 to 20 kPa at the peak

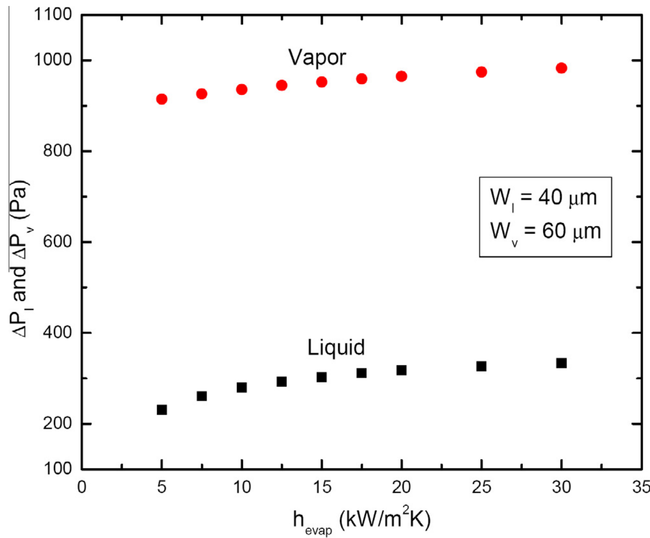

Fig. 9. Effect of the evaporation heat transfer coefficient h_{evap} on the pressure drops.

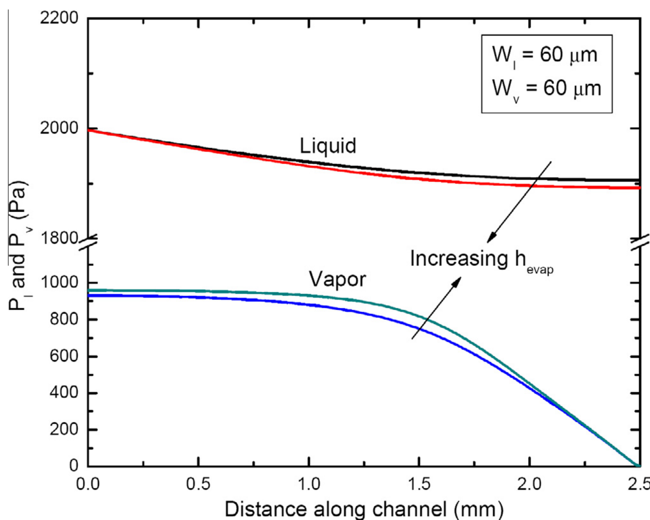

Fig. 10. The liquid and vapor pressure profile along each respective channel ($W_l = W_v$ = 60 μm).

wall heat flux. The frictional pressure loss, which is proportional to the square of the diameter, is always smaller, ranging from 38 to 10 kPa. Although larger diameter perforations are more advantageous in preventing dry out, their impact on structural robustness of the channel walls would be greater. As such, the pore diameter and porosity will need to be optimized so as to maintain high wall thermal conductance and at the same time providing sufficient capillary performance. Our analysis suggests that perforated walls with pores of diameters greater than 1 μm and porosity 10–20% can provide both solid conductance sufficient to utilize the entire wall surfaces for heat transfer and capillary pressure sufficient to overcome frictional pressure drop (along pores) at the target chip heat flux of 1000 W/cm^2.

6. Strategy for microfabrication of microchannels with perforated side walls

To achieve a high porosity while limiting its impact on the mechanical robustness, aligned perforations with nanometer scale surface roughness (<20 nm) as opposed to random pores found in aerogel-like structures are desirable. Sun et al. [34] reported an advanced photo-electrochemical (PEC) etching technique to fabricate microscale pores of very high aspect ratios (>100) through the entire thickness (>500 μm) of a silicon wafer.

Fig. 11 shows a summary of one potential fabrication approach. One first lithographically defines an array of pits on the surface of a silicon wafer. Since photo-electrochemical etching relies on highly-localized electric fields generated *internally* by photoelectrons, etching will only initiate and proceed from these pits. This allows precisely control of the location and density of perforations. The pore diameter can be controlled by tuning current density, composition of the electrolyte, wafer resistivity, and other process parameters. To obtain perforations that connect the liquid and vapor channels, a crystal-orientation-dependent electrochemical etching of silicon, illustrated as an inset in Fig. 10b [35], may be used. The silicon substrate is next etched using DRIE to form high-aspect-ratio channel walls [36,37]. Anodic bonding or other hermetic sealing approach is next used to finish the microchannels.

7. Summary

A novel cooling device with "perspiring" side walls for ultra high heat flux removal is presented in this study. The device is designed to operate with commercially available dielectric fluid Fluorinert™ FC-72. The key design features of this cooling device are:

- Use of a perforated side wall to separate the liquid and vapor microchannels
- Decoupling of the main heat conduction paths from the liquid supply paths
- Large extended surfaces for evaporation heat transfer

The separation of the liquid and vapor flow paths using perforated side walls means that both the liquid and vapor flows are in the single-phase regime. Evaporation only occurs in the arrays of micro-perforations present in the side walls of high thermal conductivity. This design enables one to circumvent limitations that

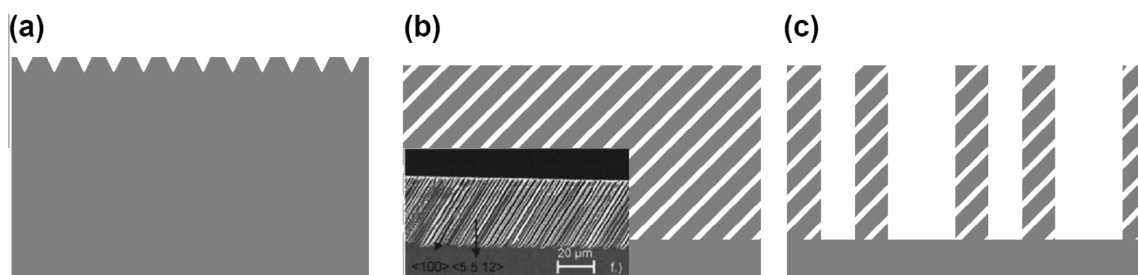

Fig. 11. A summary of processes one may employ to fabricate the perforated sidewalls of microchannels. (a) On a silicon wafer of an angled crystal direction, pits are formed in a regular array, (b) Non-vertical pores are formed deep into the wafer using PEC. The inset shows an SEM image of such inclined pores from [35], (c) The porous silicon is etched by DRIE to form the high-aspect-ratio channel sidewalls, following the lithography technique reported, for example, in [36].

have plagued previous efforts on two-phase microchannel cooling devices.

Thermo-fluid modeling results for one specific implementation of our device concept are very encouraging. The pressure drops are predicted to be <1000 Pa along 2.5 mm-long main channel sections for FC-72 and almost 2X reduction is predicted in the peak temperature rise at a peak chip heat flux of 1000 W/cm^2 when compared with single-phase microchannel flows at even higher pressure drops. The present work establishes an early feasibility of the novel phase-separated microchannel cooling concept and motivates further experimental and theoretical studies of promising embedded thermal management solutions.

Acknowledgments

The authors would like to thank Mr. Eduardo Aktinol for help with running numerical simulations and Dr. Guangyi Sun for providing Figs. 1 and 11.

References

[1] S.G. Kandlikar, Fundamental issues related to flow boiling in minichannels and microchannels, Exp. Therm. Fluid Sci. 26 (2002) 389–407.
[2] S.G. Kandlikar, High flux heat removal with microchannels – a roadmap of challenges and opportunities, Heat Transfer Eng. 26 (2005) 5–14.
[3] C.-J. Kuo, Y. Peles, Flow boiling instabilities in microchannels and means for mitigation by reentrant cavities, J. Heat Transfer 130 (2008) 072402.
[4] S. Ndao, Y. Peles, M.K. Jensen, Multi-objective thermal design optimization and comparative analysis of electronics cooling technologies, Int. J. Heat Mass Transfer 52 (2009) 4317–4326.
[5] T. Zhang, Y. Peles, J.T. Wen, T. Tong, J.-Y. Chang, R. Prasher, et al., Analysis and active control of pressure-drop flow instabilities in boiling microchannel systems, Int. J. Heat Mass Transfer 53 (2010) 2347–2360.
[6] K.H. Chang, C. Pan, Two-phase flow instability for boiling in a microchannel heat sink, Int. J. Heat Mass Transfer 50 (2007) 2078–2088.
[7] L. Zhang, E.N. Wang, K.E. Goodson, T.W. Kenny, Phase change phenomena in silicon microchannels, Int. J. Heat Mass Transfer 48 (2005) 1572–1582.
[8] J.R. Thome, V. Dupont, A.M. Jacobi, Heat transfer model for evaporation in microchannels. Part I: presentation of the model, Int. J. Heat Mass Transfer 47 (2004) 3375–3385.
[9] S.-M. Kim, I. Mudawar, Consolidated method to predicting pressure drop and heat transfer coefficient for both subcooled and saturated flow boiling in micro-channel heat sinks, Int. J. Heat Mass Transfer 55 (2012) 3720–3731.
[10] W. Qu, I. Mudawar, Flow boiling heat transfer in two-phase micro-channel heat sinks – I. Experimental investigation and assessment of correlation methods, Int. J. Heat Mass Transfer 46 (2003) 2755–2771.
[11] B. Agostini, M. Fabbri, J.E. Park, L. Wojtan, J.R. Thome, B. Michel, State of the art of high heat flux cooling technologies, Heat Transfer Eng. 24 (2007) 258–281.
[12] M.A. Ebadian, C.X. Lin, A review of high-heat-flux heat removal technologies, J. Heat Transfer 133 (2011) 110801.
[13] M.P. David, J. Miler, J.E. Steinbrenner, Y. Yang, M. Touzelbaev, K.E. Goodson, Hydraulic and thermal characteristics of a vapor venting two-phase microchannel heat exchanger, Int. J. Heat Mass Transfer 54 (2011) 5504–5516.
[14] S. Narayanan, A.G. Fedorov, Y.K. Joshi, Gas-assisted thin-film evaporation from confined spaces for dissipation of high heat fluxes, Nanoscale Microscale Thermophys. Eng. 13 (2009) 30–53.
[15] D. Francis, F. Faili, D. Babić, F. Ejeckam, A. Nurmikko, H. Maris, Formation and characterization of 4-inch GaN-on-diamond substrates, Diam. Relat. Mater. 19 (2010) 229–233.
[16] G.J. Riedel, J.W. Pomeroy, K.P. Hilton, J.O. Maclean, D.J. Wallis, M.J. Uren, et al., Reducing thermal resistance of AlGaN/GaN electronic devices using novel nucleation layers, IEEE Electron Device Lett. 30 (2009) 103–106.
[17] S.G. Bankoff, Entrapment of gas in spreading of a liquid over a rough surface, AIChE J. 4 (1958) 24–26.
[18] Y.Y. Hsu, On the size range of active nucleation cavities on a heating surface, ASME J. Heat Transfer 84 (1962) 207–216.
[19] N. Basu, G.R. Warrier, V.K. Dhir, Onset of nucleate boiling and active nucleation site density during subcooled flow boiling, J. Heat Transfer 124 (2002) 717–728.
[20] T.M. Anderson, I. Mudawar, Microelectronic cooling by enhanced pool boiling of a dielectric fluorocarbon liquid, J. Heat Transfer 111 (1989) 752.
[21] A. Bar-Cohen, P. Wang, Thermal management of on-chip hot spot, J. Heat Transfer 134 (2012) 051017.
[22] 3M Fluorinert™ Electronic Liquid FC-72 Product Information Brochure.
[23] A. Yoshinori, B.C.Y. Lu, S. Hidezumi, A four-parameter equation of state, Fluid Phase Equilib. 11 (1983) 29–48.
[24] N. Hammouda, S.C. Cheng, D.C. Groeneveld, Evaluation of thermophysical properties of Freon-22, Wärme- und Stoffübertragung 28 (1993) 387–395.
[25] A.H.N. Mousa, Study of vapor pressure and critical properties of Perfluoro-n-Hexane, J. Chem. Eng. Data. 23 (1978) 133–134.
[26] G. Thodus, P. Yoon, Viscosity of nonpolar gaseous mixtures at normal pressure, AIChE J. 16 (1970) 300–304.
[27] R.C. Reid, J.M. Prausnitz, B.E. Poling, The Properties of Gases and Liquids, fourth ed., McGraw-Hill, New York, 1987.
[28] L.I. Stiel, G. Thodos, The thermal conductivity of nonpolar substances in the dense gaseous and liquid regions, AIChE J. 10 (1964) 26–30.
[29] D. Song, G. Chen, Thermal conductivity of periodic microporous silicon films, Appl. Phys. Lett. 84 (2004) 687–689.
[30] P.E. Hopkins, C.M. Reinke, M.F. Su, R.H. Olsson, E.A. Shaner, Z.C. Leseman, et al., Reduction in the thermal conductivity of single crystalline silicon by phononic crystal patterning, Nano Lett. 11 (2011) 107–112.
[31] H.S. Abarajith, V.K. Dhir, G.R. Warrier, G. Son, Numerical simulation and experimental validation of the dynamics of multiple bubble merger during pool boiling under microgravity conditions, Ann. N.Y. Acad. Sci. 1027 (2004) 235–258.
[32] G. Son, V.K. Dhir, A level set method for analysis of film boiling on an immersed solid surface, Numer. Heat Transfer Part B: Fundam. 52 (2007) 153–177.
[33] A. Fan, R. Bonner, S. Sharratt, Y.S. Ju, An innovative passive cooling method for high performance light-emitting diodes, in: 2012 28th Annual IEEE Semiconductor Thermal Measurement and Management Symposium (SEMI-THERM), 2012, pp. 319–324.
[34] G. Sun, J.I. Hur, X. Zhao, C.-J. Kim, Fabrication of very-high-aspect-ratio micro metal posts and gratings by photoelectrochemical etching and electroplating, J. Microelectromech. Syst. 20 (2011) 876–884.
[35] M. Christophersen, J. Carstensen, S. Rönnebeck, C. Jäger, W. Jäger, H. Föll, Crystal orientation dependence and anisotropic properties of macropore formation of p- and n-type silicon, J. Electrochem. Soc. 148 (2001) E267–E275.
[36] J.-A. Paik, S.-K. Fan, C.-J. Kim, M.C. Wu, B. Dunn, Micromachining of mesoporous oxide films for microelectromechanical system structures, J. Mater. Res. 17 (2002) 2121–2129.
[37] J.-A. Paik, S.-K. Fan, H. Chang, C.-J. Kim, M.C. Wu, B. Dunn, Development of spin coated mesoporous oxide films for MEMS structures, J. Electroceram. 13 (2004) 423–428.